Elliptical Glide-Symmetric Holey Metasurfaces for Wideband Anisotropy

Antonio Alex-Amor*, Fatemeh Ghasemifard†, Guido Valerio‡, Pablo Padilla§,
José M. Fernández-González*, Oscar Quevedo-Teruel†
*Information Processing and Telecommunications Center, Technical University of Madrid, 28040 Madrid, Spain,
aalex@gr.ssr.upm.es*
†Division for Electromagnetic Engineering, School of Electrical Engineering and Computer Science, KTH Royal Institute of Technology, SE-100 44 Stockholm, Sweden
‡UR2, Laboratoire d'Électronique and Électromagnétisme, Sorbonne Université, F-75005 Paris, France
§Departamento de Teoría de la Señal, Telemática y Comunicaciones, Universidad de Granada, 18071 Granada, Spain

***Abstract*—This paper presents a mode-matching technique to study the dispersive features of periodic structures composed of glide-symmetric elliptical holes. As a difference from purely numerical methods, our formulation provides physical insight on the Floquet harmonics. At the same time, the computational cost is reduced compared to general purpose commercial software. The fields inside the holes are described by means of Mathieu functions and subsequently used to compute the full 2-D dispersion diagrams. With the presented analysis, we demonstrate that glide-symmetric periodic structures with elliptical holes offer anisotropic refractive indexes over a wide range of frequencies.**

***Index Terms*—Modal analysis, mode-matching, elliptical holes, anisotropy, glide symmetry, wideband, dispersion properties.**

I. Introduction

Metasurfaces are 2D metastructures that can be employed for the design of low-cost light-weight planar devices [1], [2]. As an example, traditional bulky and lossy beam-forming networks can be replaced by beam-scanning planar lens antennas composed of graded-index metasurfaces [3]. This fact, together with the need of higher available bandwidths, is of great interest for future communications at millimeter waves [4].

Higher symmetries [5] have demonstrated that can be used to produce unusual dispersive features of periodic structures. In particular, the dispersion of a periodic structure can be reduced with the use of glide and twist symmetries [6], [7]. Furthermore, the equivalent refractive index can be significantly increased [8]–[10]. These distinctive properties were exploited in [11], [12] for the design of fully-metallic low-loss wideband lenses applied to 5G communication systems.

The vast majority of research works in the literature that make use of metasurfaces focus on isotropic implementations. However, it is well known that anisotropy can be beneficial for some specific applications, such as wavefront transformation [13] or lens compression [14]. As an example, recently, two wideband designs with compression factors higher than 30% have been presented. The first one is a compressed Luneburg lens realized in printed circuit board (PCB) technology [15]. The second one is a compressed Maxwell fish-eye lens [16]. Both of them use of glide-symmetric elliptical holes in their designs as wideband anisotropic structures. Rectangular holes have already been proposed and analytically studied for this purpose [17], [18]. However, they are normally harder to manufacture with milling techniques, specially if the rectangular shapes are narrow. This could lead to significant deviations from the desired equivalent refractive index.

This paper focuses on the study of the intrinsic properties of periodic elliptical holes arranged in glide-symmetric configurations. For this purpose, a mode matching based on the generalized Floquet theorem is proposed. The modal functions are computed by means of the Mathieu functions. As a difference with other purely numerical approaches, physical insight in the symmetry properties of the Floquet harmonics is gained.

II. Modal Analysis

In this section, we present the mode-matching formulation that we are using to analyze the holey metasurfaces shown in Fig. 1. Figs. 1(a) and 1(b) show the glide-symmetric and non-glide-symmetric configurations, respectively. Furthermore, a cross section of the elliptical hole can be seen in Fig. 1(c). Since we are dealing with elliptical shapes, we will use an elliptical coordinate system (ξ, η, z) to take advantage of the geometry of the structure [16]. In addition, the $z = 0$ plane of the coordinate system is assumed on the glide plane.

The tangential fields on the aperture of the holes in the lower layer (at $z = -g/2$) can be expressed as

$$\mathbf{E}_t^{\mathrm{WG}}(\xi,\eta,z=-g/2) = \sum_{i=1}^{N}(1-e^{-j2k_{zi}h})\,C_i\mathbf{\Phi}_{\mathbf{i}}(\xi,\eta) \quad (1)$$

$$\mathbf{H}_t^{\mathrm{WG}}(\xi,\eta,z=-g/2) = \sum_{i=1}^{N}(1+e^{-j2k_{zi}h})\,Y_iC_i\,[\hat{\mathbf{z}}\times\mathbf{\Phi}_{\mathbf{i}}(\xi,\eta)] \quad (2)$$

where $\mathbf{\Phi}_{\mathbf{i}}(\xi,\eta)$ is the modal function that represents the i-th mode inside the hole, C_i is the coefficient of the i-th mode, Y_i is the wave admitance of the i-th mode, $(1 \pm e^{-j2k_{zi}h})$ are the reflection coefficients that take into account the short circuit at the end of the elliptical hole, h is the hole depth, $k_{zi} = \sqrt{\varepsilon_{r\mathrm{h}}k_0^2 - k_{ti}^2}$ is the wavenumber in the longitudinal

direction of the hole, $\varepsilon_{r\mathrm{h}}$ is the relative permittivity inside the hole, and k_{ti} is the transversal wavenumber.

The tangential fields in the gap region are expressed as a series of Floquet harmonics:

$$\mathbf{E}_t^{\mathrm{GAP}} = \frac{1}{d^2}\sum_{p,s} e^{-j(k_{x,p}x+k_{y,s}y)}\,\tilde{\mathbf{e}}_{t,ps}^{\mathrm{GAP}}(z) \tag{3}$$

$$\mathbf{H}_t^{\mathrm{GAP}} = \frac{1}{d^2}\sum_{p,s} e^{-j(k_{x,p}x+k_{y,s}y)}\,\tilde{\mathbf{h}}_{t,ps}^{\mathrm{GAP}}(z), \tag{4}$$

where $k_{x,p} = k_{x,0} + \frac{2\pi p}{d}$, and $k_{y,s} = k_{y,0} + \frac{2\pi s}{d}$. The integers p and s indicate the order of the Floquet harmonics. The field amplitudes of the transversal Floquet harmonics $\tilde{\mathbf{e}}_{t,ps}^{\mathrm{GAP}}(z)$, $\tilde{\mathbf{h}}_{t,ps}^{\mathrm{GAP}}(z)$ are expressed as

$$\tilde{\mathbf{e}}_{t,ps}^{\mathrm{GAP}} = \begin{pmatrix} A_{ps}^x \\ A_{ps}^y \end{pmatrix}\sin(k_{z,ps}z) + \begin{pmatrix} B_{ps}^x \\ B_{ps}^y \end{pmatrix}\cos(k_{z,ps}z) \tag{5}$$

$$\tilde{\mathbf{h}}_{t,ps}^{\mathrm{GAP}} = \begin{pmatrix} D_{ps}^x \\ D_{ps}^y \end{pmatrix}\sin(k_{z,ps}z) + \begin{pmatrix} F_{ps}^x \\ F_{ps}^y \end{pmatrix}\cos(k_{z,ps}z) \tag{6}$$

where $k_{z,ps} = \sqrt{\varepsilon_r k_0^2 - k_{x,p}^2 - k_{y,s}^2}$ and ε_r is the relative dieletric constant in the gap region. The unknown coefficients A and B are extracted by applying the continuity of the electric field at the lower and upper metallic surfaces [18], [19]. For the non-glide case:

$$\begin{pmatrix} A_{ps}^x \\ A_{ps}^y \end{pmatrix} = \frac{-\tilde{\mathbf{E}}_t^{\mathrm{WG}}}{\sin(k_{z,ps}g/2)} \tag{7a}$$

$$\begin{pmatrix} B_{ps}^x \\ B_{ps}^y \end{pmatrix} = \mathbf{0} \tag{7b}$$

For the glide case:

$$\begin{pmatrix} A_{ps}^x \\ A_{ps}^y \end{pmatrix} = \begin{cases} \mathbf{0} & p+s \quad \text{even} \\ \frac{-\tilde{\mathbf{E}}_t^{\mathrm{WG}}}{\sin(k_{z,ps}g/2)} & p+s \quad \text{odd} \end{cases} \tag{8a}$$

$$\begin{pmatrix} B_{ps}^x \\ B_{ps}^y \end{pmatrix} = \begin{cases} \frac{-\tilde{\mathbf{E}}_t^{\mathrm{WG}}}{\cos(k_{z,ps}g/2)} & p+s \quad \text{even} \\ \mathbf{0} & p+s \quad \text{odd} \end{cases} \tag{8b}$$

The coefficients D and F in (6) can be extracted by using Maxwell equations. Following the same procedure, by using the previous results and enforcing the continuity of the magnetic field at the lower surface, the following linear system of equations is derived [20]

$$\sum_{i=1}^{N} C_i\,\alpha_{ri} = 0, \qquad r = 1, ..., N \tag{9}$$

where the matrix entries α_{ri} are calculated as

$$\alpha_{ri} = jk_0\eta_0 d^2 Y_i I_{ri} + \frac{1-e^{-j2k_{zi}h}}{1+e^{-j2k_{zi}h}}\sum_{p,s}\widetilde{f}_{ps}(k_{z,ps})\beta_{ri}(\mathbf{k}_{ps}). \tag{10}$$

The dispersion equation is obtained by setting to zero the determinant of the matrix α_{ri}. Then, dispersion diagrams are calculated for different sets of $(k_{x,0}, k_{y,0})$. In (10), I_{ri} is the inner product of the r-th and i-th modal functions, $\beta_{ri}(\mathbf{k}_{ps})$ are

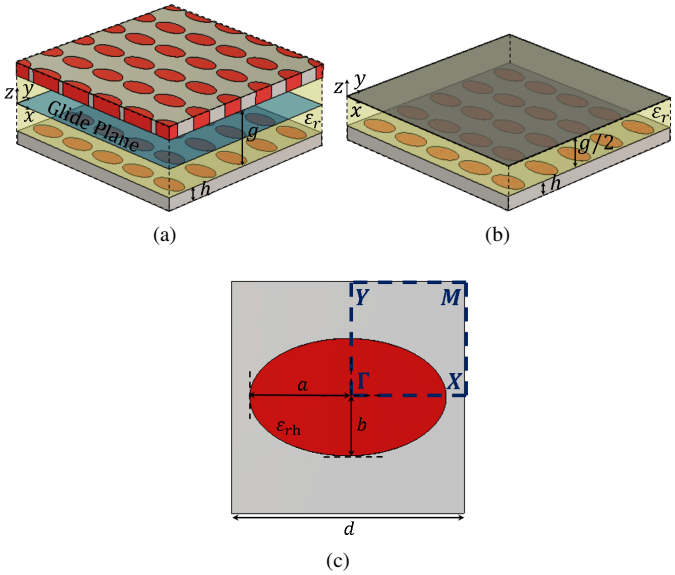

Fig. 1: Glide-symmetric (a) and non-glide-symmetric (b) 2D periodic holey structures and a cross section of the elliptical hole (c).

the entries of a matrix dependent on the 2D Fourier transform of the modal functions, and $\widetilde{f}_{ps}$ is a spectral function that distinguishes the glide and non-glide cases [20].

Interesting properties of Floquet harmonics are derived from equations (7) and (8). If we define the parity of the (p,s)-th Floquet harmonic as the parity of the number $p+s$, it can be noticed that odd harmonics in the glide case resemble to harmonics in the non-glide case. That is, the glide plane of Fig. 1(a) is equivalent to a perfect electric conductor (PEC) when $p+s$ is odd. On the other hand, the glide plane can be seen as a perfect magnetic conductor (PMC) when the number $p+s$ is even.

Unbounded structures can also be analyzed with the same formulation, as long as bounded modes are of interest. In this particular scenario, the top metallic plate is removed in both glide and non-glide structures. From the theoretical point of view, this is equivalent to set a large gap ($g \to \infty$) between both plates, which leads to imaginary values of $k_{z,ps}$ and $\widetilde{f}_{ps}(k_{z,ps})|_{g\to\infty} \to j$.

A. Modal Functions

The elliptical hole can be seen as an elliptical waveguide with a short circuit at the end. According to the theory of elliptical waveguides [21], [22], the modal functions $\mathbf{\Phi_i}(\xi,\eta)$ can be expressed by using Mathieu functions [23] and their derivatives. In the case of TM modes:

$$\phi_i^{\xi}(\xi,\eta) = \frac{1}{h_\xi}\begin{Bmatrix} Ce'_m(\xi,q_{emn})\,ce_m(\eta,q_{emn}) & \text{(even)} \\ Se'_m(\xi,q_{omn})\,se_m(\eta,q_{omn}) & \text{(odd)} \end{Bmatrix} \tag{11}$$

$$\phi_i^{\eta}(\xi,\eta) = \frac{1}{h_\xi}\begin{Bmatrix} Ce_m(\xi,q_{emn})\,ce'_m(\eta,q_{emn}) & \text{(even)} \\ Se_m(\xi,q_{omn})\,se'_m(\eta,q_{omn}) & \text{(odd)} \end{Bmatrix} \tag{12}$$

and for TE modes:

$$\phi_i^{\xi}(\xi,\eta) = \frac{1}{h_\xi}\begin{Bmatrix} Ce_m(\xi,q'_{emn})\,ce'_m(\eta,q'_{emn}) & \text{(even)} \\ Se_m(\xi,q'_{omn})\,se'_m(\eta,q'_{omn}) & \text{(odd)} \end{Bmatrix} \quad (13)$$

$$\phi_i^{\eta}(\xi,\eta) = \frac{-1}{h_\xi}\begin{Bmatrix} Ce'_m(\xi,q'_{emn})\,ce_m(\eta,q'_{emn}) & \text{(even)} \\ Se'_m(\xi,q'_{omn})\,se_m(\eta,q'_{omn}) & \text{(odd)} \end{Bmatrix} \quad (14)$$

where $ce_m(\eta,q_{emn})$, $se_m(\eta,q_{omn})$ are the even and odd angular Mathieu functions of order m, $Ce_m(\eta,q'_{emn})$ and $Se_m(\eta,q'_{omn})$ are the even and odd radial Mathieu functions of the first kind of order m, and $h_\xi = h_\xi(\xi,\eta)$ is a scale factor. The q-parameters are the n-roots of the Mathieu radial functions evaluated at the metallic wall of the waveguide, for TM modes, and the n-th roots of their first derivatives, for TE modes [16]. In the case of an elliptical waveguide, there are two propagating solutions for each mode, namely even and odd solutions. As the eccentricity of the hole approaches zero, the elliptical waveguide becomes into a regular circular waveguide. Subsequently, the two propagating solutions degenerate into a unique one, which can be expressed in terms of Bessel functions. More details related to the computation of Mathieu functions are given in the Appendix.

III. Results

In this section, we study the dispersive features and the anisotropy related to elliptical holes with the proposed mode matching. To ease the process, we set a reference unit cell and study the individual effect of the geometrical parameters that conform it. The geometrical dimensions of the reference unit cells are: $d = 4.5$ mm, $e = 0.8$, $g = 0.5$ mm, $a = 1.9$ mm, $\varepsilon_r = 1$, and $\varepsilon_{\rm rh} = 1$. All the results are validated with the eigenmode analysis of *CST Microwave Studio*.

Fig. 2 presents a comparison between the dispersion diagrams of the glide-symmetric (red) and non-glide-symmetric (blue) holey structures. In the figure, $\Gamma - \mathrm{X}$ states for propagation in x direction and $\Gamma - \mathrm{Y}$ for propagation in y direction. The results extracted with the mode matching and *CST* are represented in solid and dashed lines, respectively. As observed, there is a good agreement between both. In Fig. 2, it can be appreciated that the stop band between first and second modes disappears with the use of glide symmetry. Additionally, the propagating modes in the glide-symmetric unit cell are less dispersive. This fact leads to a constant equivalent refractive index over a large range of frequencies, which is highly desired, for example, for the design of wideband lenses [12]. The anisotropic behavior of the unit cells is also appreciated in the figure.

Fig. 3 shows the effect of inserting a dielectric material inside the holes (blue curves) and in the gap region (green curves). In both cases, the holey structure becomes denser as materials with higher relative permittivity are included.

Fig. 4 describes the influence of the size of the hole on the equivalent refractive index. In particular, different values of the semi-major axis a are considered. As illustrated, the larger the semi-major axis, the higher the equivalent refractive index. The structure becomes a parallel-plate waveguide (PPW) as the hole shrinks, and subsequently, the equivalent refractive

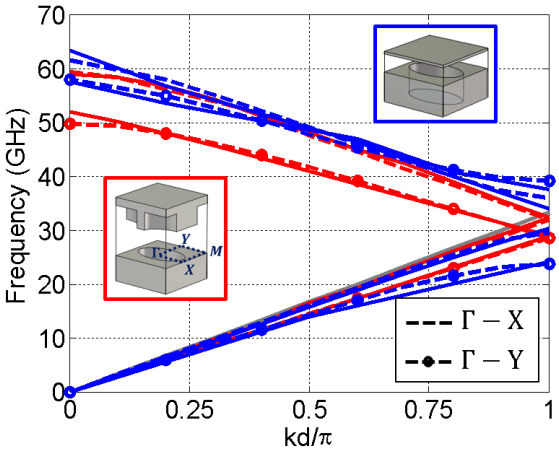

Fig. 2: Dispersion diagram of the glide-symmetric (red) and conventional (blue) holey structures. The propagation in x and y directions is illustrated. Mode matching (solid lines), *CST* (dashed lines), and light line (gray line).

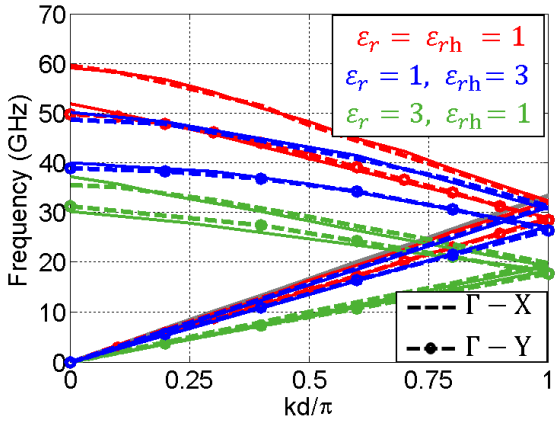

Fig. 3: Dispersion diagram of the glide-symmetric holey structure when varying the permittivity of the gap region ε_r and hole $\varepsilon_{\rm rh}$. The propagation in x and y directions is illustrated. Mode matching (solid lines), *CST* (dashed lines), and light line (gray line).

index approaches to one. Furthermore, the anisotropy of the structure is clearly evidenced in the figure. Small values of a cause irrelevant differences between both propagating directions (blue curves). However, for large values of a, there are appreciable differences between the two red curves.

Fig. 5 illustrates the effect of a varying the hole depth on the dispersion diagram of the structure. In general, deeper holes lead to higher equivalent refractive indexes. However, since the modes exponentially attenuate inside the holes [16]. There is an upper bound, approximately $h = 2.5$ mm, where increasing the hole depth has no influence on the equivalent refractive index.

Fig. 6 shows the influence of the gap height on the dispersion diagram. The interaction between top and bottom metallic layers is higher as the gap height is reduced. As a consequence, the equivalent refractive index increases. Note that there is a

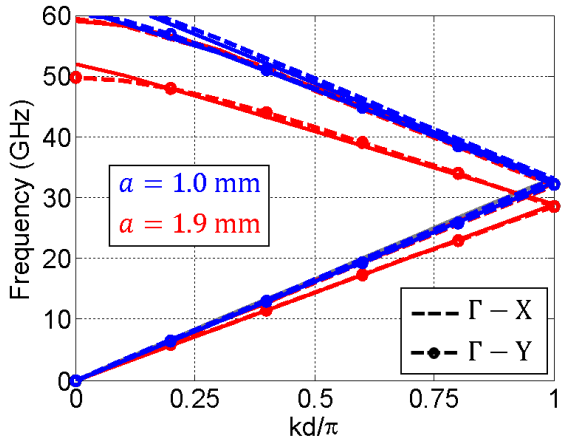

Fig. 4: Dispersion diagram of the glide-symmetric holey structure for different values of the semi-major axis a. The propagation in x and y directions is illustrated. Mode matching (solid lines), *CST* (dashed lines), and light line (gray line).

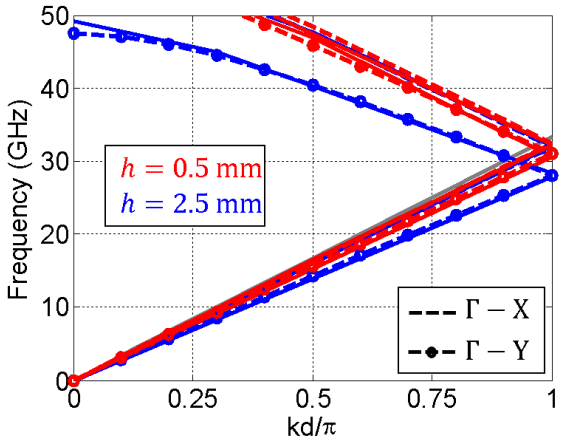

Fig. 5: Dispersion diagram of the glide-symmetric holey structure for different values of hole depth h. The propagation in x and y directions is illustrated. Mode matching (solid lines), *CST* (dashed lines), and light line (gray line).

slight discrepancy between the mode-matching technique and *CST* for small gap heights $g = 0.25$ mm. On one side, the accuracy from *CST* is not guaranteed for such extreme values of the gap. On the other side, more modes are needed inside the hole in this particular case.

In order to compare the speed of the mode-matching formulation with a standard commercial software like *CST* Microwave Studio, two simulations are carried out in the same computer (ASUS F555L; CPU: Intel Core i7-5500U @3 GHz; RAM: 8 GB). In Fig. 2, the Γ-X interval is divided in eleven equally spaced points. In the case of *CST*, the simulation time was 6 minutes and 2 seconds. In the case of our code, the simulation time was 1 minute and 40 seconds. The speed of the code could be further improved by using a complex-root-finding algorithm [25], instead of searching the minimum of the determinant in (10).

IV. Conclusion

In this paper, we analyzed the dispersive features of glide-symmetric periodic structures composed of elliptical holes with the use of a mode-matching expansion. The dispersion diagrams were computed for all the different geometrical parameters that characterizes the unit cell. We demonstrated that these structures are able to synthesize anisotropic refractive indexes over a large range of frequencies. As a consequence, they arise as a promising candidate for the fabrication of low-loss low-profile wideband lenses.

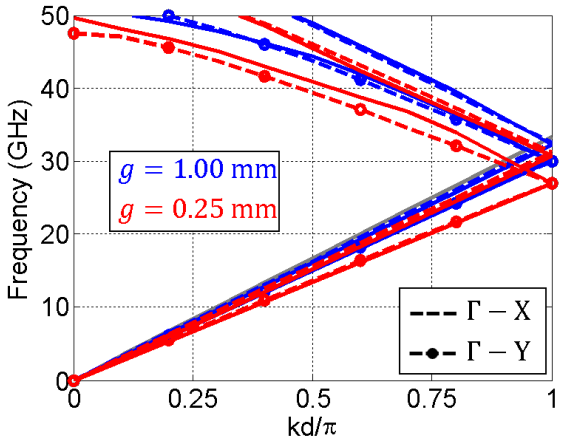

Fig. 6: Dispersion diagram of the glide-symmetric holey structure for different values of the gap height g. The propagation in x and y directions is illustrated. Mode matching (solid lines), *CST* (dashed lines), and light line (gray line).

Acknowledgment

This work was partially supported by the TIN2016-75097-P, RTI2018-102002-A-I00, and EQC2018-004988-P projects of the Spanish National Program of Research, Development, and Innovation, by project B-TIC-402-UGR18 of Junta de Andalucía, with European Union FEDER funds under the project FUTURERADIO "Radio systems and technologies for high capacity terrestrial and satellite communications in an hyperconnected world" (project number TEC2017-85529-C3-1-R), by The French National Research Agency Grant Number ANR-16-CE24-0030, by the Vinnova project High-5 (2018-01522) under the Strategic Programme on Smart Electronic Systems, and by the Stiftelsen Åforsk project H-Materials (18-302).

Appendix

Computation of Mathieu Functions

Even and odd angular Mathieu functions ce_m and se_m can be expanded as Fourier series with coefficients that are dependent on the q-parameters. Thus, for $m \geq 0$:

$$ce_{2m}(\eta, q) = \sum_{n=0}^{\infty} A_{2n}^{(2m)}(q) \cos 2n\eta \tag{15}$$

$$ce_{2m+1}(\eta, q) = \sum_{n=0}^{\infty} A_{2n+1}^{(2m+1)}(q) \cos(2n+1)\eta \tag{16}$$

$$se_{2m+1}(\eta, q) = \sum_{n=0}^{\infty} B_{2n+1}^{(2m+1)}(q) \sin(2n+1)\eta \tag{17}$$

$$se_{2m+2}(\eta, q) = \sum_{n=0}^{\infty} B_{2n+2}^{(2m+2)}(q) \sin(2n+2)\eta \tag{18}$$

The expansion coefficients A and B are calculated through recurrence formulas by substituting equations (15)-(18) in the wave equation associated to the elliptical waveguide [22]. As an example, for $ce_{2m}(\eta, q)$ [23]:

$$a_{2m}(q)A_0^{(2m)} - qA_2^{(2m)} = 0 \tag{19a}$$

$$\left(a_{(2m)}(q) - 4n^2\right) A_{2n}^{(2m)} - q\left(A_{2n+2}^{(2m)} + 2A_{2n-2}^{\ (2m)}\right) = 0, \quad n \geq 1 \tag{19b}$$

where $a_{2m}(q)$ is a characteristic number related to the parameter q. It can be estimated according to the continuous-fraction equation depicted in [24].

Even and odd radial Mathieu functions can be directly computed from angular Mathieu functions (15)-(18) according to the relations

$$Ce_m(\xi, q) = ce_m(j\xi, q) \tag{20}$$

$$Se_m(\xi, q) = -j\, se_m(j\xi, q) \tag{21}$$

When the eccentricity of the ellipse is zero ($e = 0$), the elliptical waveguide transforms into a common circular waveguide and all the roots q are null. As a consequence, the Mathieu functions transform into

$$ce_m(\eta, 0) = \cos(m\phi) \tag{22a}$$

$$se_m(\eta, 0) = \sin(m\phi) \tag{22b}$$

$$Ce_m(\xi, 0) = Se_m(\xi, 0) = \left(\frac{\pi}{2}\right)^{\frac{1}{2}} J_m(k_o\rho) \tag{22c}$$

where J_m is the Bessel function of the first kind and (z, ρ, ϕ) are the coordinates of a cylindrical coordinate system.

REFERENCES

[1] C. L. Holloway, E. F. Kuester, J. A. Gordon, J. O'Hara, J. Booth and D. R. Smith, "An Overview of the Theory and Applications of Metasurfaces: The Two-Dimensional Equivalents of Metamaterials," *IEEE Antennas Propag. Mag.*, vol. 54, no. 2, pp. 10-35, 2012.

[2] O. Quevedo-Teruel *et al.*, "Roadmap on metasurfaces," *J. Opt.*, vol. 21, no. 7, 2019.

[3] O. Quevedo-Teruel, J. Miao, M. Mattsson, A. Algaba-Brazalez, M. Johansson, L. Manholm, "Glide-symmetric fully-metallic Luneburg lens for 5G Communications at Ka-band", in *IEEE Antennas Wireless Propag. Lett.*, vol. 17, no. 9, pp. 1588-1592, Sept. 2018.

[4] S. Maci, G. Minatti, M. Casaletti, and M. Bosiljevac, "Metasurfing: Addressing waves on impenetrable metasurfaces," *IEEE Antennas Wireless Propag. Lett.*, vol. 10, pp. 1499-1502, 2011.

[5] A. Hessel, Ming Hui Chen, R. C. M. Li and A. A. Oliner, "Propagation in periodically loaded waveguides with higher symmetries," in *Proceedings of the IEEE*, vol. 61, no. 2, pp. 183-195, Feb. 1973.

[6] Q. Chen, F. Ghasemifard, G. Valerio, and O. Quevedo-Teruel, "Modeling and dispersion analysis of coaxial lines with higher symmetries," *IEEE Trans. Microw. Theory Techn.*, vol. 66, no. 10, pp. 4338-4345, Oct. 2018.

[7] F. Ghasemifard, M. Norgren, and O. Quevedo-Teruel, "Twist and polar glide symmetries: An additional degree of freedom to control the propagation characteristics of periodic structures," *Sci. Rep.*, vol. 8, Jul. 2018, Art. no. 11266.

[8] A. Palomares-Caballero, P. Padilla, A. Alex-Amor, J. Valenzuela-Valdés, and O. Quevedo-Teruel, "Twist and Glide Symmetries for Helix Antenna Design and Miniaturization," *Symmetry*, vol. 11, no. 349, 2019.

[9] A. Palomares-Caballero, A. Alex-Amor, J. Valenzuela-Valdes, F. Luna and P. Padilla, "Phase Shifter for Millimeter-Wave Frequency Range Based on Glide Symmetric Structures,"*13th European Conference on Antennas and Propagation (EuCAP 2019)*, Krakow, Poland, 2019, pp. 1-4..

[10] A. Palomares-Caballero, A. Alex-Amor, P. Padilla, F. Luna, and J. Valenzuela-Valdés, "Compact and Low-Loss V-band Waveguide Phase Shifter Based on Glide-Symmetric Pin Configuration," *IEEE Access*, vol. 7, pp. 31297-31304, 2019.

[11] O. Quevedo-Teruel, M. Ebrahimpouri and F. Ghasemifard, "Lens Antennas for 5G Communications Systems," *IEEE Commun. Mag.*, vol. 56, no. 7, pp. 36-41, July 2018.

[12] O. Quevedo-Teruel, M. Ebrahimpouri, M. Ng Mou Kehn, "Ultra Wide Band Metasurface Lenses Based on Off-Shifted Opposite Layers", *IEEE Antennas Wireless Propagation Letters*, vol.15, pp. 484-487, 2016.

[13] G. Gok and A. Grbic, "A Printed Beam-Shifting Slab Designed Using Tensor Transmission-Line Metamaterials," *IEEE Trans. Antennas Propag.*, vol. 61, no. 2, pp. 728-734, 2013.

[14] D. A. Roberts, N. Kundtz, and D. R. Smith, "Optical lens compression via transformation optics," Opt. Express, vol. 17, no. 19, pp. 16535-16542, Sept. 2009

[15] M. Ebrahimpouri, O. Quevedo-Teruel, "Ultra-wideband Anisotropic Glide-symmetric Metasurfaces," *IEEE Antennas Wireless Propag. Lett.*, vol. 18, no. 8, pp. 1547-1551, Aug. 2019.

[16] A. Alex-Amor, F. Ghasemifard, G. Valerio, M. Ebrahimpouri, P. Padilla, J. M. Fernández-González, O. Quevedo-Teruel, "Glide-Symmetric Metallic Structures with Elliptical Holes for Lens Compression," submitted to *IEEE Trans. Microw. Theory Techn.*

[17] F. J. García-Vidal, L. Martín-Moreno, and J. B. Pendry, "Surfaces with holes in them: new plasmonic metamaterials," *J. Opt. A: Pure Appl. Opt.*, vol. 7, 2005.

[18] G. Valerio, F. Ghasemifard, Z. Sipus, O. Quevedo-Teruel, "Glide-Symmetric All-Metal Holey Metasurfaces for Low-Dispersive Artificial Materials: Modeling and Properties," *IEEE Trans. Microw. Theory Techn.*, vol. 66, no. 7, pp. 3210-3223, July 2018.

[19] F. Ghasemifard, Periodic Structures with Higher Symmetries: Analysis and Applications. PhD Thesis, KTH Royal Institute of Technology, 2018.

[20] F. Ghasemifard, M. Norgren, O. Quevedo-Teruel, G. Valerio, "Analyzing Glide-Symmetric Holey Metasurfaces Using a Generalized Floquet Theorem," *IEEE Access*, vol. 6, pp. 71743-71750, 2018.

[21] L. J. Chu. "Electromagnetic Waves in Elliptic Hollow Pipes of Metal," *J. Appl. Phys.*, vol. 9, pp. 583, 1938.

[22] J. G. Kretzschmar, "Wave Propagation in Hollow Conducting Elliptical Waveguides," *IEEE Trans. Microw. Theory Techn.*, vol. MTT-18, no. 9, 1970.

[23] N. W. McLachlan. *Theory and Application of Mathieu Functions*. Dover Publications, Reprint edition, 1964.

[24] G. B. Arfken, H. J. Weber, F. E. Harris. *Mathematical Methods for Physicists: A Comprehensive Guide*. Elsevier, 7th Edition, 2012.

[25] V. Galdi and I. M. Pinto, "A simple algorithm for accurate location of leaky-wave poles for grounded inhomogeneous dielectric slabs," *Microw. Opt. Technol. Lett.*, vol. 24, no. 2, pp. 135-140, 2000